

Observations of Turbulence in the Ocean Surface Boundary Layer: Energetics and Transport

GREGORY P. GERBI*

Woods Hole Oceanographic Institution–Massachusetts Institute of Technology, Woods Hole, Massachusetts

JOHN H. TROWBRIDGE, EUGENE A. TERRAY, ALBERT J. PLUEDDEMANN, AND TOBIAS KUKULKA

Woods Hole Oceanographic Institution, Woods Hole, Massachusetts

(Manuscript received 1 May 2008, in final form 15 December 2008)

ABSTRACT

Observations of turbulent kinetic energy (TKE) dynamics in the ocean surface boundary layer are presented here and compared with results from previous observational, numerical, and analytic studies. As in previous studies, the dissipation rate of TKE is found to be higher in the wavy ocean surface boundary layer than it would be in a flow past a rigid boundary with similar stress and buoyancy forcing. Estimates of the terms in the turbulent kinetic energy equation indicate that, unlike in a flow past a rigid boundary, the dissipation rates cannot be balanced by local production terms, suggesting that the transport of TKE is important in the ocean surface boundary layer. A simple analytic model containing parameterizations of production, dissipation, and transport reproduces key features of the vertical profile of TKE, including enhancement near the surface. The effective turbulent diffusion coefficient for heat is larger than would be expected in a rigid-boundary boundary layer. This diffusion coefficient is predicted reasonably well by a model that contains the effects of shear production, buoyancy forcing, and transport of TKE (thought to be related to wave breaking). Neglect of buoyancy forcing or wave breaking in the parameterization results in poor predictions of turbulent diffusivity. Langmuir turbulence was detected concurrently with a fraction of the turbulence quantities reported here, but these times did not stand out as having significant differences from observations when Langmuir turbulence was not detected.

1. Introduction

Turbulence in the ocean surface boundary layer results both from shear and convective instabilities similar to those found near rigid boundaries and from instabilities related to surface gravity waves, wave breaking, and Langmuir turbulence. While rigid-boundary turbulence has been extensively studied for nearly a century, turbulence driven by surface waves has been addressed in detail only in the past two decades. In particular, the relationships of turbulent fluxes and en-

ergies to wave breaking and Langmuir turbulence continue to be uncertain. Observations (Santala 1991; Plueddemann and Weller 1999; Terray et al. 1999b; Gerbi et al. 2008), laboratory experiments (Veron and Melville 2001), and large eddy simulations (LESs; Skillingstad and Denbo 1995; Mc Williams et al. 1997; Noh et al. 2004; Li et al. 2005; Sullivan et al. 2007) have shown that vertical mixing is more efficient in wave-driven turbulence than in rigid-boundary turbulence alone. That is, given the same fluxes of momentum and buoyancy at the boundary, vertical gradients in the surface boundary layer are smaller, and turbulent viscosities and diffusivities are larger, than would be expected in a similarly forced flow beneath a rigid boundary. However, the relationship between the diffusivities and the forcing has not been established.

The energetics of turbulence provide important diagnostic and predictive tools and form the basis for most common turbulence closure models used in the ocean (Jones and Launder 1972; Mellor and Yamada 1982; Wilcox 1988; Burchard and Baumert 1995; Umlauf et al.

* Current affiliation: Institute of Marine and Coastal Sciences, Rutgers, The State University of New Jersey, New Brunswick, New Jersey.

Corresponding author address: Gregory P. Gerbi, Institute of Marine and Coastal Sciences, Rutgers, The State University of New Jersey, 71 Dudley Rd., New Brunswick, NJ 08901-8521.
E-mail: gerbi@marine.rutgers.edu

2003; Umlauf and Burchard 2003; Kantha and Clayson 2004). Because of the difficulty of measuring turbulent fluxes and kinetic energy in a wavy environment, observations of the energetics of ocean surface boundary layer turbulence have generally been confined to dissipation rates of turbulent kinetic energy (TKE) and the vertical velocity variance. Most studies have found dissipation rates of TKE that were enhanced over those expected beneath rigid boundaries (Kitaigorodskii et al. 1983; Agrawal et al. 1992; Anis and Moum 1995; Terray et al. 1996; Drennan et al. 1996; Greenan et al. 2001; Soloviev and Lukas 2003; Gemmrich and Farmer 2004; Stips et al. 2005; Feddersen et al. 2007; Jones and Monismith 2008b). These studies have successfully related the enhanced dissipation rates to fluxes of energy from the wave field, and have suggested that in the depth range where wave-breaking-induced turbulence is dominant, the vertical integral of the dissipation rate is equal to the amount of energy that the waves have lost to breaking. Turbulence closure models have dealt with the increased dissipation by assuming that breaking waves inject TKE at the sea surface and that that TKE is dissipated as it is transported downward by turbulence and pressure work (Craig and Banner 1994; Craig 1996; Terray et al. 1999b; Burchard 2001; Umlauf et al. 2003; Kantha and Clayson 2004). These models, in turn, predict that in the presence of breaking waves, the magnitude of TKE increases substantially within several wave heights of the surface relative to purely rigid-boundary turbulence. This prediction of enhanced TKE is consistent with the observations of D'Asaro (2001) and Tseng and D'Asaro (2004), who made measurements of the vertical component of TKE with Lagrangian floats and found it to be enhanced relative to expectations from rigid-boundary scaling. In a study similar to the one described here, Kitaigorodskii et al. (1983) measured two components of TKE beneath waves in a lake. They also found enhanced TKE near the surface, but their sums of only the vertical and down-wave horizontal components precluded a more complete analysis of the relationship between TKE, dissipation rate, and effective diffusivity.

A simple conceptual model has emerged from previous studies in the ocean surface boundary layer (Fig. 1). Nearest the surface, in what we refer to as the wave breaking layer, is the part of the boundary layer in which waves break and form turbulence. Below that, in what Stips et al. (2005) called the wave-affected surface layer (WASL), the boundary layer is affected by turbulence that is transported downward from the surface, but wave breaking does not inject turbulence directly. The WASL scaling relations developed by Terray et al. (1996) assume that the dissipation profile in the wave

breaking layer is vertically uniform, an assumption that has been shown by Gemmrich and Farmer (2004) to break down very near the sea surface. In the WASL, near its upper boundary, the TKE balance is thought to be between dissipation and transport; at deeper depths, the relative importance of the transport of TKE from the surface diminishes and the TKE dynamics approach a production–dissipation balance, similar to that expected in rigid-boundary turbulence.

The present study of turbulence energetics was undertaken as a companion to a study of turbulent fluxes in the surface boundary layer (Gerbi et al. 2008) and was designed to address the following areas: closure of the TKE budget, our understanding of the relationship between TKE and dissipation, and the determination of the role of wave breaking in setting the turbulent diffusivity in the boundary layer. In the process, an analytical model of the vertical structure of TKE (Craig 1996; Burchard 2001) is tested. In the following, section 2 describes the observations, and section 3 shows the results of those observations. Section 4 analyzes the results in comparison to other observations and analytic studies, and section 5 offers conclusions. An appendix describes our method of estimating the dissipation rate of TKE using Eulerian measurements of turbulence in the presence of unsteady advection due to surface gravity waves.

2. Methods

a. Data collection

The observations reported here were made using instruments deployed in the ocean and atmosphere at the Martha's Vineyard Coastal Observatory's (MVCO's) Air–Sea Interaction Tower, during the Coupled Boundary Layers and Air Sea Transfer low winds experiment (CBLAST-Low) in the fall of 2003. The tower is located about 3 km south of Martha's Vineyard, Massachusetts, in approximately 16 m of water (Fig. 2). Currents are dominated by semidiurnal tides and are dominantly shore parallel (east–west). The mean wind direction is from the southwest. Velocity measurements were made by six Sontek 5-MHz Ocean Probe acoustic Doppler velocimeters (ADV) deployed at 1.7, 2.2, and 3.2 m below the mean sea surface (Fig. 3). The 3.2-m sensor also contained a pressure sensor and was only used to compute wave statistics, not turbulence statistics. High-frequency temperature measurements were made with fast-response thermistors located within the ADV sample volumes, and the mean temperature and density were measured with Seabird MicroCATs at 1.4-, 2.2-, 3.2-, 4.9-, 6-, 7.9-, 9.9-, and 11.9-m depths. The measurements were described in detail by Gerbi et al. (2008).

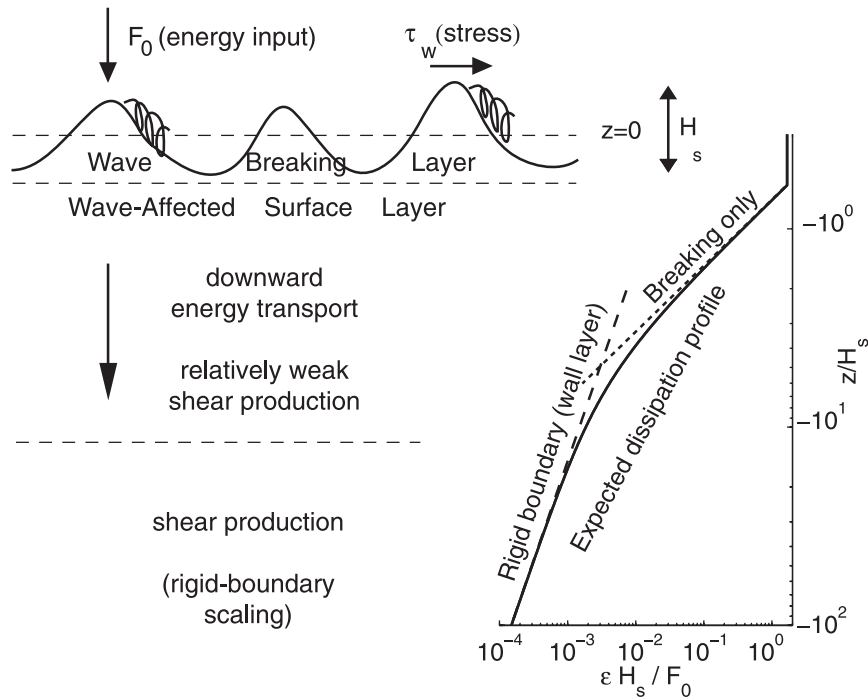


FIG. 1. Schematic description of the boundary layer structure, including the wave breaking layer, above-trough level, and wave-affected surface layer, which is thought to approach rigid-boundary scaling at sufficient depths. The cartoon of the normalized dissipation profiles shows a constant region in the wave breaking layer, dissipation dominated by the transport of TKE at the top of the wave-affected surface layer, and a transition to rigid-boundary scaling at deeper depths. Here, z is the vertical coordinate, H_s is the significant wave height, ϵ is the dissipation rate, τ_w is the wind stress, and F_0 is the wind energy input to the waves.

Velocities in each 20-min burst were rotated into streamwise coordinates based on the mean velocity for that burst. In this system, x and y are the coordinates in the downstream and cross-stream directions, respectively, and z is the vertical coordinate, positive upward, with $z = 0$ at the burst-mean height of the sea surface, which was determined from pressure measurements. Instantaneous values of velocity in the (x, y, z) directions are denoted by (u, v, w) . Conceptually, velocity observations were decomposed into mean, wave, and turbulent components as

$$\mathbf{u} = \bar{\mathbf{u}} + \tilde{\mathbf{u}} + \mathbf{u}', \quad (1)$$

where the boldface type denotes a vector quantity and $\mathbf{u} = (u, v, w)$. Overbars represent a time mean over the length of the burst, $(\tilde{u}, \tilde{v}, \tilde{w})$ denote wave-induced perturbations, and (u', v', w') denote turbulent perturbations. By definition, below the wave troughs, the means of the wave and turbulent quantities are zero. Conceptually, the turbulent velocity component includes all unsteady motions not correlated with surface wave motions, including, potentially, Langmuir turbulence and

the coherent vortices that have been observed to persist after waves have broken in laboratory experiments (Melville et al. 2002). In practice, the signals were decomposed in the time domain into mean parts and perturbation parts. The perturbation parts of the signal were further separated in frequency space into turbulent motions and wave motions.

Because of measurement sensitivity, estimates of the dissipation rate and TKE were limited to a subset of environmental conditions. We used several criteria to choose acceptable data for inclusion in our analysis. As stated by Gerbi et al. (2008), the instruments were mounted on the west side of the Air–Sea Interaction Tower; so to eliminate distortion from flow through the tower, we analyzed data only for flows from the west. Because this study focuses on boundary layer processes, we analyzed data only when the bottom of the surface boundary layer [defined as the depth at which the temperature difference from the shallowest MicroCAT exceeded 0.02°C (Lentz 1992)] was at least 3.2 m below mean sea level. The ADVs have finite sensitivity and as a criterion for eliminating large wave orbital velocities, we only took bursts for which the vertical velocity

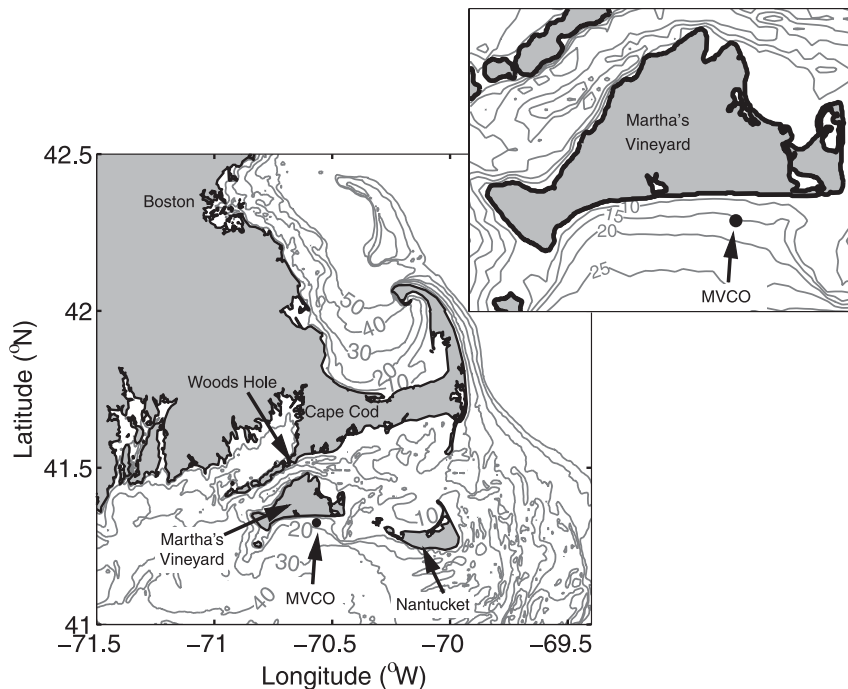


FIG. 2. Maps showing the location of MVCO. Contours show isobaths between 10 and 50 m. The inset map shows the area in the immediate vicinity of the study site. [This figure is reprinted from Gerbi et al. (2008).]

variance was less than $0.025 \text{ m}^2 \text{ s}^{-2}$. The oscillating motions due to surface waves caused the wakes of the ADVs to be advected into the sample volumes of the instruments at times when the mean current was not strong enough to sweep the wakes from the ADVs before the waves carried them back to the sample volumes. Therefore, bursts were rejected when the wakes were likely to be advected back into the sample volumes for even a small fraction of the time. In practice, for estimates of the dissipation rate and TKE, we required $U_d/\sigma_{U_d} > 3$, where U_d is the magnitude of the mean velocity and σ_{U_d} is the velocity variance in the downstream direction. This restriction left times when the significant height of the wind waves was less than 1 m (Fig. 4). Finally, there are times when white noise dominates the measurements at frequencies above the wave band. These were identified during the estimation of the dissipation rates and were removed as described in section 2b.

The following arguments suggest that the TKE estimates at the depths of the ADVs are likely not influenced by bottom boundary layer processes. Laboratory experiments and observations of unstratified boundary layers at rigid boundaries (Klebanoff 1955; Corrsin and Kistler 1955; McPhee and Smith 1976) have shown that in the depths of interest to this study, the TKE varies roughly linearly with distance from the boundary such that

$$\frac{q^2}{|\tau|/\rho_0} = a \left(1 - \frac{\xi}{\delta}\right), \quad (2)$$

where $q^2 = 1/2(\overline{u'^2} + \overline{v'^2} + \overline{w'^2})$ is the burst-mean turbulent kinetic energy, $|\tau|$ is the magnitude of the shear stress at the boundary, ρ_0 is a reference density, a is a constant between about 1 and 10, ξ is the distance from the boundary, and δ is the boundary layer thickness. The TKE in a wave-affected boundary layer is expected to be larger than that in a rigid-boundary boundary layer, so (2) can be used to give a conservative estimate of the sensitivity of the ADVs to bottom boundary layer turbulence. If one assumes that each boundary layer fills the entire water column ($\delta = h$), and that the boundary layers interact in a linear fashion, the ratio of the TKE expected to be present at a depth z from turbulence associated with the top and bottom boundary layers is

$$\frac{q_{\text{top}}^2}{q_{\text{bottom}}^2} = \frac{|\tau|_{\text{top}} (1 + z/h)}{|\tau|_{\text{bottom}} (-z/h)}. \quad (3)$$

During this study, the surface and bottom stresses were of similar magnitudes, and the ratio $(1 + z/h)/(-z/h)$ is about 7 for the depths of the ADVs. A similar analysis using exponential fits to TKE profiles in open-channel flow by Nezu and Rodi (1986) leads to a depth-dependent scaling factor of about 3.6 rather than 7 for the ADV

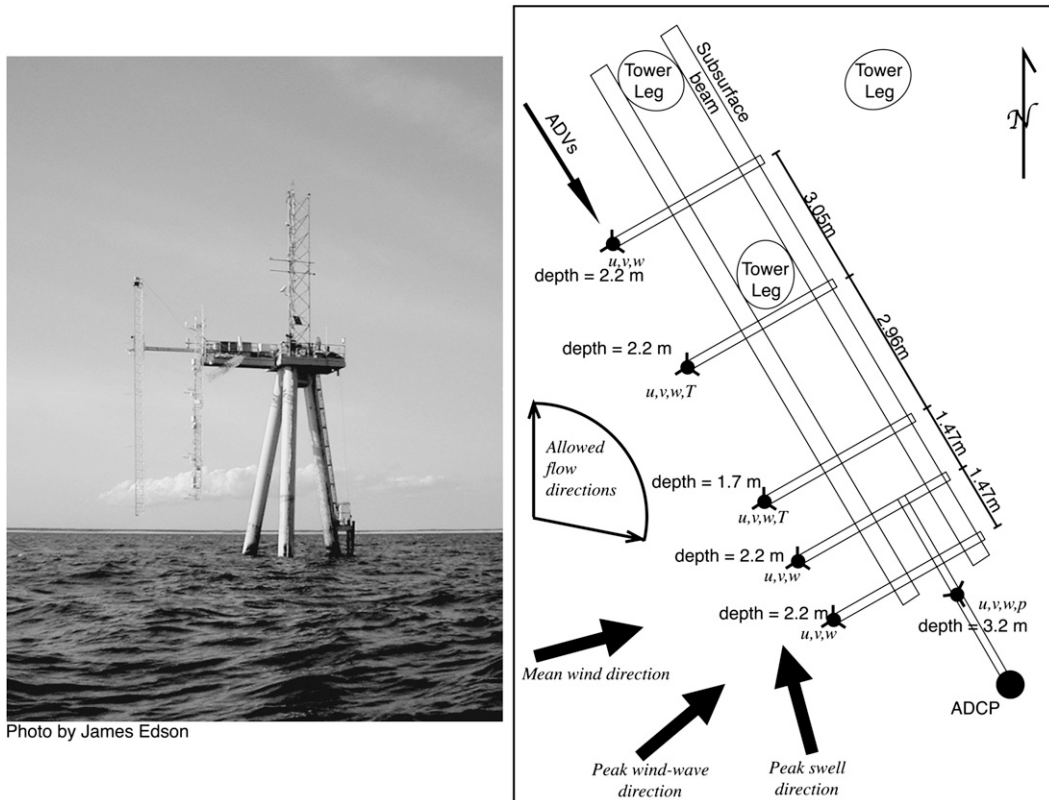


FIG. 3. Photograph, looking north, and schematic plan-view drawing of the Air-Sea Interaction Tower at MVCO. In the photograph, the platform is 12 m above the sea surface. In the schematic diagram of the instrument tower, ellipses represent the tilted tower legs (which join at the platform). Small filled circles with three arms each represent ADVs and thermistors. The large filled circle represents the middepth ADCP. Mean wind and wave directions are shown by boldfaced arrows, and the range of flow directions (0° – 120°) used in this study is shown to the left. [This figure is reprinted from Gerbi et al. (2008).]

depths. The ratio q_{top}^2/q_{bottom}^2 in (3) is greater than 1 in about 95% of the bursts for which estimates of the bottom stress are available, and it is usually much greater than 1, with a median of about 11. Because observations of bottom stress are limited and because the averaged effects of bottom boundary layer turbulence observed at the ADVs are minimal, observations in this study are not restricted based on the magnitude of the bottom stress.

The measurement period lasted about 34 days, with about 2500 bursts. The restriction on flow direction eliminated about 60% of those bursts. Of the remaining bursts, about 35% were eliminated by the vertical velocity variance threshold, and an additional 20% were eliminated by the boundary layer thickness criterion. Finally, the U_d/σ_{U_d} threshold and the noise limit removed about 90% of the remaining observations. Thus, the energy and dissipation estimates shown in this study account for about 6% of the times when the mean flow was in a direction favorable to making turbulence measurements, and the bulk of that restriction was due

to wave velocities being large enough that turbulent wakes from the ADVs were advected through the measurement volumes.

b. Terms in the TKE budget

We estimated or placed bounds on most of the terms in a horizontally homogeneous turbulent kinetic energy budget:

$$\frac{\partial q^2}{\partial t} = \frac{\tau}{\rho_0} \cdot \left[\frac{\partial \bar{\mathbf{u}}}{\partial z} + \frac{\partial \mathbf{u}_s}{\partial z} \right] + \frac{g}{\rho_0} \overline{\rho' w'} - \varepsilon - \frac{\partial F}{\partial z}, \quad (4)$$

where t is time, $\tau = -\rho_0(\overline{u'w'}, \overline{v'w'}, 0)$ is the Reynolds shear stress vector, ρ' is the density perturbation, $\mathbf{u}_s = (u_s, v_s, 0)$ is the vector Stokes drift of the surface gravity waves, g is acceleration due to gravity, ε is the dissipation rate of TKE, and F is the vertical transport of TKE. The left-hand side of (4) is the rate of change of TKE. The first term on the right side is the production of turbulent kinetic energy by extraction of energy from the shear of the mean flow and from the wave field via

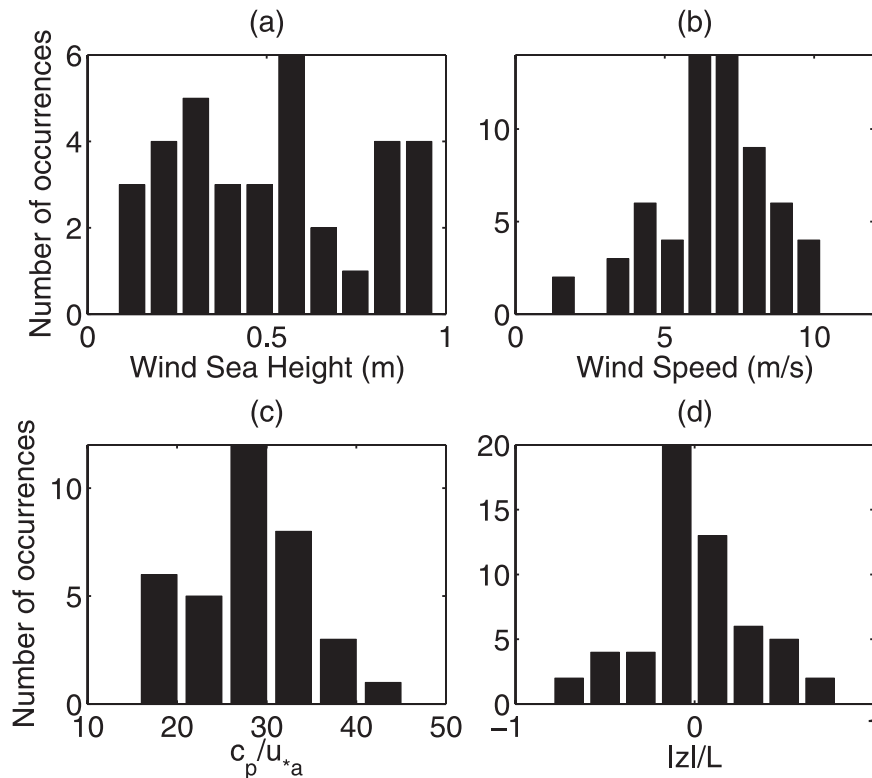


FIG. 4. Environmental conditions during times of dissipation and TKE observations: (a) the significant height of the wind waves, (b) the wind speed at 10-m height, (c) the age of the wind waves, and (d) the Monin–Obukhov parameter at the lower (2.2 m) ADV computed from surface fluxes. Four points with values between -6 and 10 have been omitted from the histogram of $|z|/L$.

Stokes drift shear. The second term is the production or dampening of TKE by buoyancy forcing.

This TKE equation assumes no mean vertical flow. Because Gerbi et al. (2008) were able to close the heat and momentum budgets without wave contributions to the fluxes, terms like $\overline{u\tilde{w}}$ and $\overline{u'w'}$ are expected not to be important in the shear production of TKE (first term on the right-hand side). The transport of TKE F contains the turbulent transport terms, $\overline{p'w'}/\rho_0 + 1/2\overline{\mathbf{u}' \cdot \mathbf{u}'w'}$, where p is pressure, and may also contain additional wave–turbulence interaction terms. We were able to estimate $\partial q^2/\partial t$, $(\boldsymbol{\tau}/\rho_0) \cdot (\partial \mathbf{u}_s/\partial z)$, $(g/\rho_0)\overline{\rho'w'}$, and ε , and place an upper bound on $(\boldsymbol{\tau}/\rho_0) \cdot (\partial \overline{\mathbf{u}}/\partial z)$. As will be discussed later, we were unable to separate wave motions from turbulence motions adequately to estimate the magnitude of the transport term F . Methods for computing the other terms in the TKE budget are described below.

The rate of change of the turbulent kinetic energy was estimated from one-sided finite differences between 20-min bursts when we had successive estimates of q^2 . A detailed discussion of how we computed TKE is found in section 2c.

The shear production terms were estimated using local stresses computed from cospectra as described by Gerbi et al. (2008). We estimated the Stokes drift shear from directional wave spectra (described in section 2e). The Stokes drift shear in each direction is

$$\begin{aligned} \frac{\partial u_s}{\partial z} &= \int_0^{2\pi} d\theta \cos \theta \int_0^{\omega_{\max}} d\omega D_{\eta\eta} \omega k F'_s, \\ \frac{\partial v_s}{\partial z} &= \int_0^{2\pi} d\theta \sin \theta \int_0^{\omega_{\max}} d\omega D_{\eta\eta} \omega k F'_s, \end{aligned} \quad (5)$$

where

$$F'_s = \frac{2k \sinh [2k(z+h)]}{\sinh^2(kh)}, \quad (6)$$

and h is the water depth, ω is the radian frequency, k is the radian wavenumber, θ is the direction, and $D_{\eta\eta}(\omega, \theta)$ is the directional wave spectrum of sea surface displacement. We were unable to estimate the mean shear production term because we did not have sufficiently precise estimates of shear. Previous work (Gerbi et al. 2008) suggests that the shear in the surface boundary

layer is smaller than that predicted by Monin–Obukhov similarity theory, so local Monin–Obukhov theory (using local estimates of buoyancy and momentum fluxes) was used to estimate an upper bound on the shear in the wind direction. Crosswind shears were assumed to be negligible. Multiplying the mean shear upper bound by the momentum flux gives an upper bound on the production of TKE by shear instabilities of the mean flow, and multiplying the Stokes drift shear by the momentum flux gives an estimate of the local production by Stokes shear instabilities.

Buoyancy production was estimated from temperature flux measurements using a burst-mean correlation between the temperature and density fluctuations so that the density flux is estimated as

$$\overline{\rho'w'} = \alpha_T \overline{T'w'}. \quad (7)$$

Here, T is temperature and $\alpha_T = \partial\rho/\partial T$ was estimated from the linear regression of 1-min averages of ρ and T . Using a constant value of $\alpha_T = -0.3 \text{ kg m}^{-3} \text{ }^\circ\text{C}^{-1}$ changes the results by only a small amount and does not affect the conclusions. There were a limited number of times when estimates of both ε and $\overline{T'w'}$ could be made from spectra, so for this TKE budget, estimates of $\overline{T'w'}$ were determined from a heat budget as described by Gerbi et al. (2008).

To estimate the dissipation rate of the turbulent kinetic energy, we used inertial range scaling (Tennekes and Lumley 1972) and included the effects of unsteady advection on the spectra. Feddersen et al. (2007) have extended the kinematic model of Lumley and Terray (1983) for estimating dissipation rates at frequencies above the wave band. Their methods are used here but with a slightly different numerical scheme. For clarity, indicial notation is used here. The standard deviations of the wave velocities are σ_1 , σ_2 , and σ_3 ; the 3-direction is vertical, and the 1- and 2-directions are in the principal horizontal axes of the wave motions. In the inertial range, at frequencies sufficiently far above the wave band, the frequency spectrum $S_{33}(\omega)$ and dissipation rate ε are related as [similar to Feddersen et al. (2007)]

$$S_{33}(\omega) = J_{33}\alpha \varepsilon^{2/3} \omega^{-5/3} + n, \quad (8)$$

where α is the Kolmogorov constant, taken here to be 1.5, and n is noise, taken to be constant. In steadily advected turbulence with no wave effects, for two-sided spectra,

$$J_{33} = \frac{12}{55} \frac{1}{U_d^{2/3}}, \quad (9)$$

returning the well-known relation for the vertical velocity spectra (Kolmogorov 1941a,b; Batchelor 1982). In turbulence advected by unsteady wave motions, the magnitude of the inertial range is a function of the standard deviations of the wave velocity and the mean velocity:

$$J_{33} = J_{33}(\sigma_1, \sigma_2, \sigma_3, \bar{u}_1, \bar{u}_2). \quad (10)$$

The details for calculating J_{33} are provided in the appendix. Dissipation rates were estimated by finding the least squares fit of (8) to S_{33} between frequencies of $\omega = 2\pi$ and $10\pi \text{ rad s}^{-1}$, which are above the wave band but below the range usually dominated by noise. As mentioned in section 2a, bursts were not included in the analysis if noise dominated the vertical velocity spectra in the inertial range. Equation (8) gives estimates of ε and the white noise spectral density n . Bursts were rejected by requiring that the noise be less than one-half of the magnitude of the best-fit spectrum at $\omega = \omega_{\min} = 2\pi \text{ rad s}^{-1}$. For inclusion in the analysis, this requires for estimates from S_{33} ,

$$n < J_{33}\alpha \varepsilon^{2/3} \omega_{\min}^{-5/3}. \quad (11)$$

In contrast to the spectra of vertical velocities, the spectra of horizontal velocities were too contaminated by noise at high frequencies to allow for estimation of the dissipation rates from S_{11} and S_{22} .

In the flux of TKE F , the pressure work $\overline{p'w'}$ is notoriously difficult to estimate with conventional instrumentation, and no attempt was made to compute this term. Estimates were made of the transport of TKE by turbulence $\overline{q^2w'}$ for the part of the flux explained by low-wavenumber turbulent motions. A low-pass Butterworth filter was used to separate wave motions from turbulent motions. The low-frequency limit of the wave band was identified by determining when pressure measurements, using linear wave theory, explained at least 30% of the energy in the vertical velocity spectrum (Gerbi et al. 2008). The filter was constructed with a passband frequency of 2/3 times this wave-band cutoff frequency and a stopband frequency of 4/3 times the wave-band cutoff frequency. Using these cutoff frequencies limited the observations to structures with spatial scales roughly 2–3 m and larger. Higher-frequency information was not included in these flux estimates because of contamination due to surface gravity waves.

c. Turbulent kinetic energy estimates

Estimating TKE in the presence of surface waves is difficult, and a spectral approach was used to separate turbulent motions from wave motions. In brief, this approach ignored velocity fluctuations in the wave band

and accounted for unsteady advection effects below and above the wave band to estimate the frequency spectra that would have been observed under steady advection. These spectra were transformed to wavenumber space by assuming that the turbulence field was frozen, and a model turbulence spectrum was used to interpolate between the high- and low-frequency portions of the observed spectra (Fig. 5). Fitting this model spectrum to the observed spectra allowed for the estimation of the variance explained by turbulent velocity fluctuations. The reader not interested in the details of this calculation can proceed to section 2d below.

As was discussed regarding dissipation rates, the high-frequency part of the turbulence spectrum is elevated by unsteady advection due to surface waves. We used J_{33} from (10) and (A13) to estimate and remove the effects of the wave advection from the inertial ranges. At these frequencies ($2\pi-10\pi \text{ rad s}^{-1}$), the vertical velocity frequency spectrum observed during unsteady advection was adjusted to a “steady” form according to

$$S_{ww}^{(\text{steady})} = \frac{S_{ww}^{(\text{unsteady})}}{J_{33}} \left(\frac{12}{55} \frac{1}{U_d^{2/3}} \right). \quad (12)$$

This transformation lowered the height of the observed above-wave-band spectra by 5%–10%.

The above-wave-band portions of S_{uu} and S_{vv} were more problematic because they were dominated by measurement noise and because inertial ranges (with $S \propto \omega^{-5/3}$) could not be identified. To account for this, we constructed artificial tails for the high frequencies of the horizontal velocity spectra. These tails were constructed using the dissipation estimates from S_{ww} , such that in the inertial range the following isotropic relationships hold (e.g., Tennekes and Lumley (1972)):

$$S_{uu} = \frac{9}{55} \frac{\alpha}{U_d^{2/3}} \epsilon^{2/3} \omega^{-5/3} \quad \text{and} \quad (13)$$

$$S_{vv} = \frac{12}{55} \frac{\alpha}{U_d^{2/3}} \epsilon^{2/3} \omega^{-5/3}, \quad (14)$$

where u is in the downstream direction and v is in the cross-stream direction. Previous observations of the dissipation rate in the wavy surface layer (Terray et al. 1996) have shown that the relationship between S_{uu} and S_{ww} is robust.

In addition to elevating the high-frequency parts of the spectra, unsteady advection also affects the turbulence spectra at frequencies immediately below the wave band by drawing them down relative to what is expected in steady advection. At sufficiently low frequencies, however, the unsteady effect is minimal (Lumley and Terray 1983) and the spectrum observed in

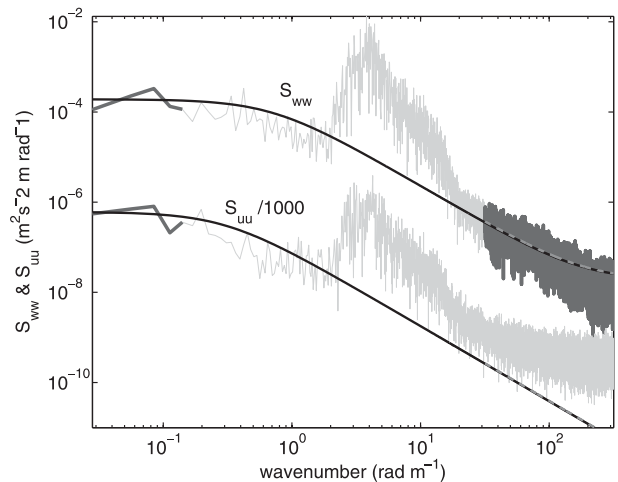


FIG. 5. Example autospectra of velocity fluctuations for a 20-min burst: light gray, observed; dark gray (thick lines), observations used in model fitting; black, best fit to full spectrum model; and dashed, best fit to the inertial range model. The top spectrum is S_{ww} and the bottom spectrum is S_{uu} , reduced for clarity by a factor of 1000. As explained in the text, because of noise, the inertial ranges of S_{uu} and S_{vv} used in the fitting were determined from the inertial range w spectra and not from observations of u and v . To minimize the effects of unsteady advection due to surface gravity waves at frequencies below the wave band, only the lowest wavenumbers were used in the model fit in the below-wave-band part of the spectrum.

unsteady motion approaches the steady form. To avoid as much of the unsteady effect as possible below the wave band, the analysis included only motions with periods greater than about 3.5 min, using only the five lowest nonzero frequencies in the below-wave band part of the fits. Following Lumley and Terray [(1983), their Eqs. (4.9) and (4.10)] a two-dimensional model of unsteady advection was used to verify that at these long periods unsteady advection has minimal impact on the frequency spectra of the turbulence.

After the wave band and some of the below-wave-band portions of the spectra were removed, the remaining frequency spectra consist of the observed spectra at frequencies $0.005-0.03 \text{ rad s}^{-1}$ and the adjusted (or constructed) spectra at frequencies $2\pi-10\pi \text{ rad s}^{-1}$. For comparison to the model spectrum, we transformed the frequency spectra into wavenumber spectra using Taylor’s hypothesis (Taylor 1938):

$$k = \frac{\omega}{U_d}. \quad (15)$$

The model that was fit to the observed spectra is similar to that used by Gerbi et al. (2008) to estimate turbulent covariances. The one-dimensional wavenumber spectrum of turbulence is described by a simple model similar to turbulence spectra observed in the laboratory (Hannoun et al. 1988) and in the atmosphere

(Kaimal et al. 1972), and one that can be obtained by integrating the von Kármán spectrum in two dimensions (Fung et al. 1992):

$$P_{\gamma\gamma}(k) = \sigma_\gamma^2 A \frac{1/k_{0\gamma}}{1 + (k/k_{0\gamma})^{5/3}}. \quad (16)$$

For two-sided spectra,

$$A = \frac{5}{6\pi} \sin\left(\frac{3\pi}{5}\right),$$

where the subscript γ is u , v , or w , and $k_{0\gamma}$ is the spectral roll-off wavenumber for the γ component of the velocity. Making a two-parameter least squares fit of this model spectrum to observations allows for the estimation of σ_γ^2 and $k_{0\gamma}$, which describe the variance and the spatial scale of the energy-containing eddies, respectively. To give all parts of the model fit equal weight, the fitting was performed in log–log space (Fig. 5). As was the case in the study of turbulent fluxes (Gerbi et al. 2008), about 17% of the spectra that we attempted to fit with the model could not be fit with geophysically reasonable parameters. These spectra are excluded from this analysis.

This method of estimating TKE is tested in two ways. First, to determine whether the below-wave-band parts of the spectrum have a strong adverse effect on the best-fit model, dissipation rates obtained from the full-model fit are compared to those obtained from fitting only the above-wave-band parts of the spectra. Second, to determine whether these energy estimates are consistent with previous energy estimates using different methods, the estimates of the vertical velocity variance are compared to estimates made by D’Asaro (2001) and Tseng and D’Asaro (2004). By taking the high-wavenumber limit of (16), equating it to (13), and assuming frozen turbulence, the variance and roll-off wavenumber estimates can be combined to give an estimate of the dissipation rate:

$$\varepsilon = k_{0u} \left(\frac{55 \sigma_u^2 A}{9 \alpha} \right)^{3/2}, \quad (17)$$

with similar equations for v and w . The dissipation estimates from the full model fit are in good agreement with the estimates from the inertial range, biased low by an average of only 10% (Fig. 6). Full model fits (not shown) that include higher frequencies below the wave band give less agreement between the full-spectrum and inertial range estimates of the dissipation rate than do the full model fits using only the frequencies below 0.03 rad s⁻¹. The spectral estimates of the vertical velocity variance are consistent with those made by D’Asaro

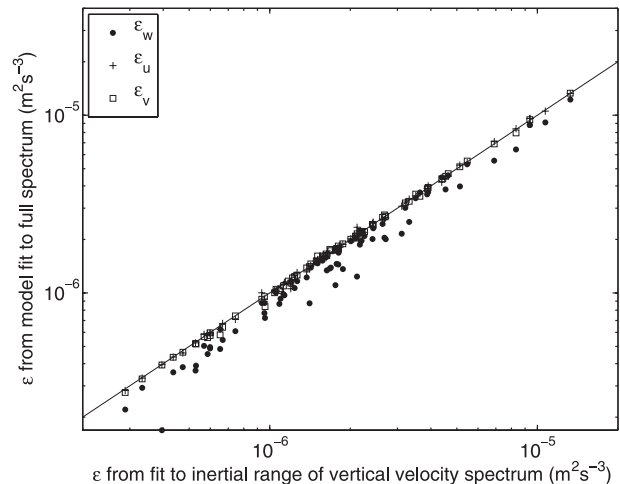


FIG. 6. Comparison of estimates of the dissipation rate as a test of internal consistency of two-parameter fits of the model spectrum to observed spectra: vertical axis, estimates derived from fitting the model to the full spectrum (17); horizontal axis, estimates derived using only the inertial range of the vertical velocity spectrum (8). The line is 1:1. Symbols are dissipation estimates from full-model fits to each component of velocity.

(2001) and Tseng and D’Asaro (2004) using autonomous floats (Fig. 7). These two comparisons suggest that our spectral fitting method gives reliable estimates of the turbulent kinetic energy in the surface boundary layer.

d. Langmuir turbulence detection

The strength of the Langmuir turbulence, as reflected by the root-mean-square (RMS) amplitude of the surface velocity convergence, was estimated using a special-purpose acoustic Doppler current profiler (ADCP). This “fanbeam” ADCP (Plueddemann et al. 2001) was mounted on the seafloor about 50 m offshore of the Air–Sea Interaction Tower (Fig. 3). The instrument uses conventional ADCP electronics but has a modified transducer head that creates four narrow-azimuth beams (3° spaced 30° apart in the horizontal plane). These beams are broad in elevation (24°), intersect the sea surface at a shallow angle, and have an intensity-weighted return that is dominated by scattering in the upper 1–3 m when bubbles injected by breaking waves are sufficiently strong (Crawford and Farmer 1987; Smith 1992). Standard range gating produces successive sampling cells along the sea surface with dimensions of about 2.5 m (along beam) × 5 m (cross beam). The along-beam aperture of the measurements varies with wind and wave conditions (Plueddemann et al. 2001). For this study, a conservative, fixed aperture of 90 m was used. The ADCP ping rate was 1 Hz, with 56-ping ensembles recorded every minute.

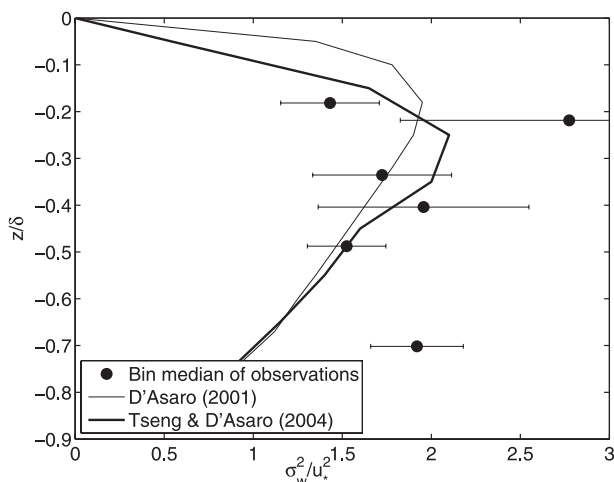


FIG. 7. Comparison of the vertical distribution of vertical velocity variances measured in this study and those measured by autonomous floats from D'Asaro (2001) and Tseng and D'Asaro (2004). Error bars show 2 standard errors from the median in each bin.

Each beam was processed separately to produce a velocity anomaly for 20-min time intervals and resolved spatial scales (5–90 m along beam). A temporal high-pass filter with a half-power point at 40 min was applied first. This removed the tidal variability that dominated the raw velocities. The high-passed velocities were then detrended in time and range within contiguous 20-min processing windows, after which wavenumber spectra were computed for each time step. The mean spectrum for the 20-min window was integrated over spatial scales from 40 to 5 m, giving a velocity variance. The square root of this quantity, denoted V_{rms} , was recorded for each beam.

When V_{rms} was above the estimated noise level of 1.2 cm s^{-1} , the velocity anomaly often showed coherent structures (subparallel lines of convergence and divergence on a time–range plot and a broadly peaked wavenumber spectrum) characteristic of Langmuir turbulence being advected past the sensor (Smith 1992; Plueddemann et al. 1996, 2001). A detailed investigation of Langmuir turbulence is beyond the scope of this paper. Instead, V_{rms} was used as an indicator of whether Langmuir turbulence was present during time periods when terms in the TKE budget could be estimated. A threshold of $V_{\text{rms}} > 1.8 \text{ cm s}^{-1}$ was found to be a robust indicator of the coherent structures in the fanbeam ADCP data and, in the results that follow, is used as the threshold for declaring that Langmuir turbulence was clearly detectable in the surface velocity field. Smaller-scale or weaker Langmuir turbulence could have been present at times when this V_{rms} threshold was not exceeded.

e. Directional wave spectra and windsea

To estimate Stokes drift and the characteristics of the windsea and swell, we used directional wave spectra derived from observations made with a 1200-kHz Teledyne RD Instruments (RDI) Workhorse ADCP located at the 12-m isobath, about 1 km shoreward of the Air–Sea Interaction Tower. The directional spectra were computed from contiguous 20-min segments of 2-Hz ADCP data using the RDI WavesMon software package. WavesMon uses a maximum likelihood estimator and linear wave theory to estimate the directional wave spectrum from individual beam velocities (Terray et al. 1999a; Strong et al. 2000; Krogstad et al. 1988). Comparisons of ADCP-derived frequency spectra to those of a laser altimeter mounted on the tower (Churchill et al. 2006) showed that the ADCP was influenced by noise at high frequencies. A cutoff of 2.5 rad s^{-1} was applied for the spectra used in this study. Because of the vertical decay (6) of the Stokes drift shear, the lack of directional wave spectra at frequencies above 2.5 rad s^{-1} is unlikely to lead to underestimates of Stokes shear production at the depths of the TKE estimates by more than 10%. Significant wave-height estimates from the ADCP and from the ADVs at the tower were well correlated, with a squared correlation coefficient of 0.87. This, combined with the qualitative agreement of one-dimensional spectra from the tower and the ADCP, suggests that the wave field at the ADCP location was similar to that at the tower.

The study region is influenced both by locally generated wind waves and by remotely generated swell (Fig. 8). The regional geography limits the swell to being predominantly from the south, and the presence of Martha's Vineyard causes wind wave development at the site to depend on wind direction. During periods of weak wind forcing, the surface wave spectrum is often dominated by swell. To isolate the locally generated windsea from swell components, the method of Hanson and Phillips (2001) was applied by Churchill et al. (2006) using the APL Waves software package developed at the Applied Physics Laboratory of Johns Hopkins University. Spectral partitioning included the isolation of all peaks above a predefined threshold, identification of the windsea peak using the observed wind speed and direction, and the coalescence of adjacent swell peaks when certain criteria were met (Hanson and Phillips 2001). The output of the analysis includes the height, period, and direction of the windsea and one or more swell systems, as well as traditional measures of significant wave height and spectral peak period. During times of weak wind forcing, or when the expected windsea peak was at frequencies greater than 2.5 rad s^{-1} ,

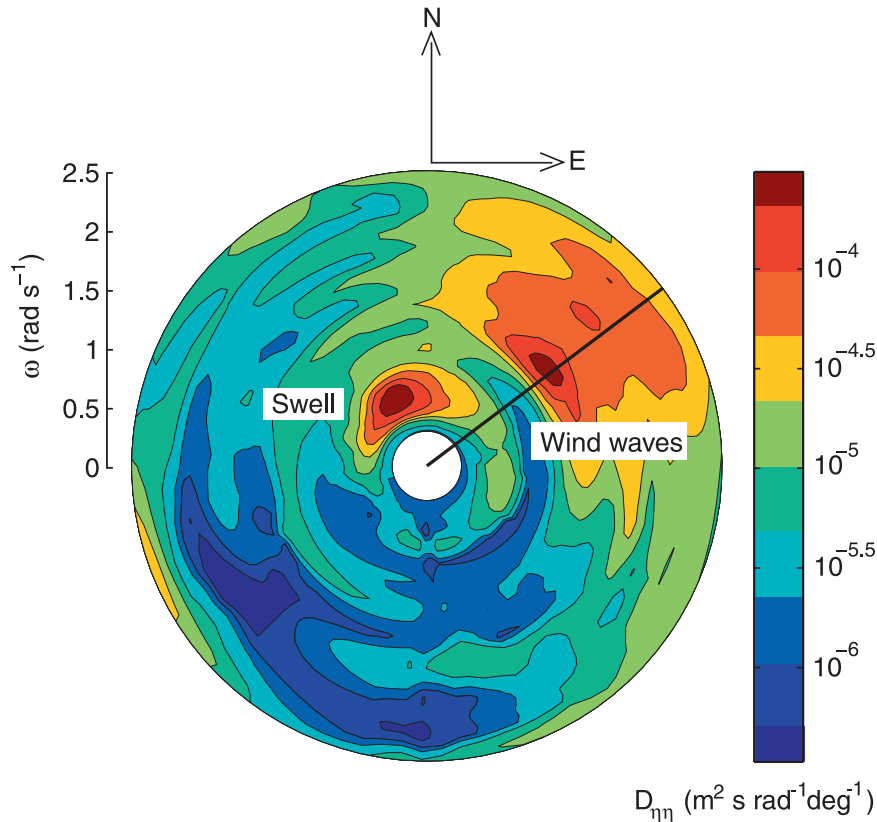


FIG. 8. Directional wave spectrum from a 20-min burst on 8 Oct 2003, showing distinct peaks due to swell and wind waves. The line at 54° from north shows the wind direction. In this burst, as is common during the study, the swell propagates toward the north-northwest and the wind waves propagate toward the northeast.

no windsea was identified. Unless otherwise noted, all subsequent analyses use windsea significant height H_s and windsea wave age c_p/u_{*a} , where c_p is the phase speed of the peak of the wind wave spectrum, $u_{*a} = \sqrt{\tau_w/\rho_a}$ is the friction velocity in the air, τ_w is the wind stress, and ρ_a is the density of the air. Times when no windsea could be identified are excluded from the analysis at times when wave height is required.

f. Wind energy input

For turbulence generated by the wave breaking, the amount of energy transferred from the wave field to the turbulence has been suggested to play a role in setting dissipation rates, total TKE, and TKE flux (Terray et al. 1996; Drennan et al. 1996; Craig and Banner 1994; Craig 1996; Burchard 2001). Following Terray et al. (1996), we assume that most of the energy transferred from the wind to the waves is rapidly transferred from the waves to the water column, and that the wave field grows slowly compared to the rate of energy input from the wind. Thus, estimating the energy input from the wind to the waves is a proxy for estimating the energy input

from the waves to the turbulence. To estimate the wind energy input, previous studies have used the directional wave spectrum and a growth rate formulation (Plant 1982; Donelan and Pierson 1987; Donelan 1999; Donelan et al. 2006). Unfortunately, this wave growth estimate is sensitive to frequencies above the 2.5 rad s^{-1} resolution of our directional spectra, so we were unable to make accurate estimates of the wind energy input by integrating the spectra. In addition, the growth rate formulas are untested in the complex wave fields present during this study, so it is not clear that even perfect directional wave spectra would have allowed precise estimates of wind energy input to the wave field.

Instead of using the growth rate formulas, we follow a simpler approach. Previous studies (Craig and Banner 1994; Terray et al. 1996; Sullivan et al. 2007) have related energy input to wave age via

$$F_0 = -u_*^3 G_\tau, \quad (18)$$

where $u_* = \sqrt{\tau_w/\rho_0}$ is the water-side friction velocity and G_τ is an empirical function of the wave age. Values

for G_t are not well constrained. For all but extremely young seas (when waves have just begun growing toward equilibrium with the wind), Terray et al. (1996) found values between about 90 and 250. Other observational studies have found an even wider range of values, including Jones and Monismith (2008a) ($G_t = 60$) and Feddersen et al. (2007) ($G_t = 250$). Because our observations are in a wave-age range in which Terray et al. (1996) found G_t to be roughly constant, we use a single value for all our observations. We find that $G_t = 168$ gives the best fit of the observations to the dissipation rate scaling of Terray et al. (1996).

3. Results

a. Conditions of observation

The standard deviation of the tidal displacement of the sea surface was 0.35 m, so measurement depths were between about 1.35 and 2.55 m. Wind speeds during the study period were between 1 and 11 m s⁻¹, with a mean of about 6.7 m s⁻¹. The wind waves in our study were relatively mature, with ages c_p/u_{*a} between 18 and 44 (Fig. 4). Previous studies (McWilliams et al. 1997; Li et al. 2005) have shown that Langmuir turbulence usually occurs at turbulent Langmuir numbers, $La_t = \sqrt{u_* u_{s0}} < 0.7$, where u_{s0} is the downwind component of the Stokes drift at the surface and $u_* = \sqrt{\tau_w/\rho_0}$. The computation of La_t is sensitive to the maximum frequency resolved by the directional wave spectra, and the observed spectra at frequencies below 2.5 rad s⁻¹ lead to values of La_t that are usually between 0.5 and 1.5, with few values less than 0.7. However, it is likely that wind wave energy extends to higher frequencies than 2.5 rad s⁻¹ and that the true values of La_t are more often near or below 0.7. As will be seen later, given the weak forcing in which we could measure TKE, few of our observations were made at times when Langmuir turbulence was detected.

The Monin–Obukhov parameter $|z|/L$ was used to characterize the influence of the buoyancy forcing during the study. The quantity $|z|/L$ is defined as

$$\frac{|z|}{L} = \frac{\overline{g\rho'w'\kappa|z|}}{\rho_0(\tau/\rho_0)^{3/2}}, \quad (19)$$

where κ is von Kármán's constant, $|z|$ is the absolute value of the distance from the sea surface, and the Monin–Obukhov length is $L = \rho_0(\tau/\rho_0)^{3/2}/(\kappa g \overline{\rho'w'})$. Positive values of L denote stable buoyancy forcing and negative values denote unstable buoyancy forcing. Surface values of the buoyancy flux and stress were used to compute L , and the buoyancy flux was calculated

from heat fluxes measured in the atmosphere, including sensible, latent, upwelling and downwelling longwave radiation, and incident and reflected shortwave radiation. Most of the observations were made during times of weak buoyancy forcing, with $|z|/L < 1$. Stratification was also used to characterize the influence of the buoyancy. Nearly all of the measurements were made in weak stratification, with density differences between MicroCATs at 1.4- and 3.2-m depths less than 0.01 kg m⁻³ for 90% of the observations. The remaining 10% of the observations were made when density differences were less than 0.03 kg m⁻³ (see Thomson and Fine 2003).

b. Dissipation

Observations of the dissipation rate of TKE show enhancement over those expected in turbulence near a rigid boundary. With significant wave heights less than 1 m and measurement depths between 1.35 and 2.55 m, according to the scaling of Terray et al. (1996), our measurements were confined to the wave-affected surface layer (Fig. 1) and did not reach into the breaking layer above $z = z_b = 0.6H_s$. As was found by previous researchers examining this part of the water column (Agrawal et al. 1992; Anis and Moum 1995; Terray et al. 1996; Drennan et al. 1996; Greenan et al. 2001; Soloviev and Lukas 2003; Stips et al. 2005; Feddersen et al. 2007; Jones and Monismith 2008b), the observed dissipation rate of the turbulent kinetic energy is larger than what would be expected for rigid-boundary turbulence (Fig. 9). The dissipation rates follow the scaling of Terray et al. (1996), which assumes that turbulent kinetic energy is extracted from the surface waves via breaking and dissipates as it is transported downward (Thompson and Turner 1975; Craig and Banner 1994). The scaling in the WASL is

$$\varepsilon = 0.3 \frac{-F_0 H_s}{z^2} = 0.3 \frac{G_t u_*^3 H_s}{z^2}. \quad (20)$$

Within the context of the TKE equation, (4), this scaling ignores the growth and production terms and balances the dissipation with the divergence of the flux of TKE.

In the complex seas in this study, the significant wave height could be that associated with the full spectrum (dominated by swell) or that computed from the energy in the wave field driven by the local wind (wind waves). The choice of significant wave height in (20) affects the agreement of the observations with the scaling (Fig. 9). For the data to collapse to the scaling, the significant wave height of the wind waves must be used, rather than that of the full spectrum. It has also been suggested that the wavelength of the dominant wind wave can be used as a depth scale (Drennan et al. 1996). Because the

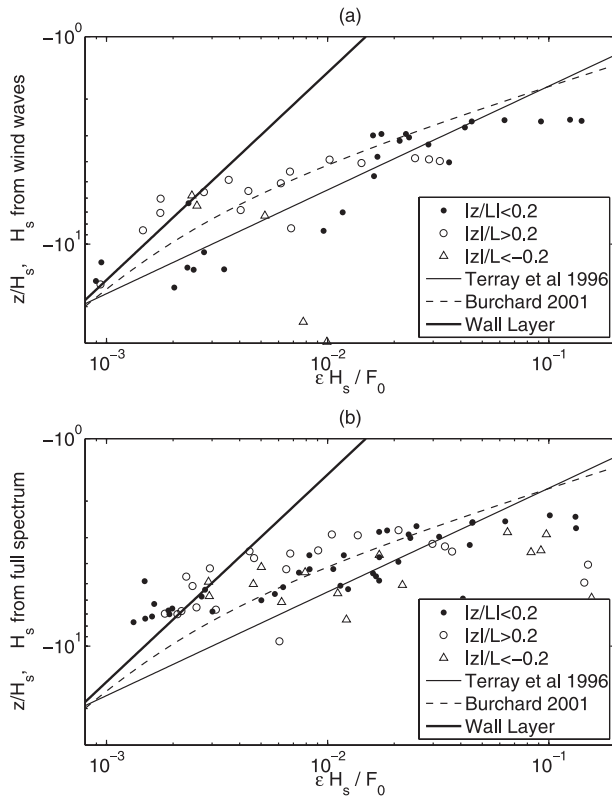


FIG. 9. Observations of the dissipation rate, normalized as suggested by Terray et al. (1996). Depth is normalized by (a) the significant wave height associated with the wind waves and (b) the significant wave height computed from the full spectrum (usually dominated by swell). The thick lines are the expected dissipation rates using neutral rigid-boundary scaling, the thin lines show the scaling of Terray et al. (1996), and the dashed lines show the model predictions of Burchard (2001) and Craig (1996), with $c_\mu^o = 0.2$ and $\mathcal{L} = 0.4$ (explained in section 4a). The symbols indicate different stability regimes, characterized by the Monin–Obukhov parameter, $|z/L|$: $|z/L| < 0.2$ is near neutral, $|z/L| > 0.2$ is slightly stable, and $|z/L| < -0.2$ is slightly unstable. Most measurements were made when $|z/L| < 1$, so that buoyancy is not the dominant forcing mechanism.

wavelength and significant height of the wind waves are correlated, our results are also consistent with this suggestion.

c. TKE balance

Although the enhanced dissipation rate has been observed many times in the surface boundary layer, the association of enhanced dissipation with the flux of TKE from a nonlocal source has remained an attractive, but, to our knowledge, untested, suggestion. By estimating (or bounding, in the case of shear production) terms in the TKE equation, we find that local production of TKE is not sufficient to balance the observed dissipation rates (Fig. 10). The buoyancy production and Stokes shear

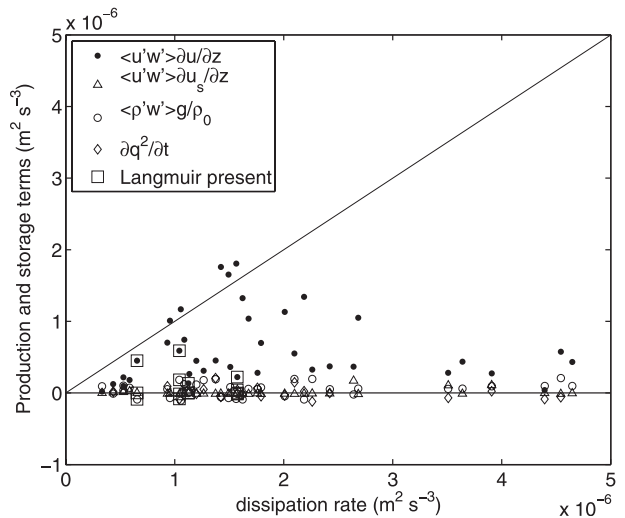


FIG. 10. Estimates or upper bounds (on shear production only) on production, growth, and dissipation terms in the TKE budget. The dissipation term is usually larger than the sum of the other terms, suggesting that the terms not included here—the transport terms—are important in the TKE balance. Boxes show times when Langmuir turbulence was detected.

production terms both are consistently small compared to dissipation. We were unable to measure the storage term for all bursts because we did not always have sequential estimates of TKE, but when measurable, the storage term is also small compared to dissipation. Only the upper bound on the shear production occasionally approaches the magnitude of the dissipation rate at some times of low dissipation rates, suggesting that a local balance could hold. For most of the observations, the dissipation rate greatly exceeds even that upper bound on the shear production. Mean values of each term are given in Table 1.

Equation (20) can be integrated vertically to give a prediction of TKE flux past each depth. By assuming a balance between the dissipation and the transport of TKE, ignoring contributions from local production, and assuming that the TKE diminishes to zero at depth, one gets

$$\int_{-\infty}^z dz' \varepsilon = \int_{-\infty}^z dz' \frac{\partial F}{\partial z'} = F(z) = \frac{-0.3F_0H_s}{z}. \quad (21)$$

Our estimates of the TKE transport explained by low-frequency motions are much smaller than (21), suggesting that pressure work is important or that most of

TABLE 1. Mean values of each term in the TKE equation.

ε	$\overline{u'w'\partial\bar{u}/\partial z}$ (upper bound)	$\overline{u'w'\partial u_s/\partial z}$	B	$\partial q^2/\partial t$
1.83×10^{-6}	6.11×10^{-7}	4.95×10^{-9}	4.70×10^{-8}	4.33×10^{-9}

the TKE transport involves motions in or above the wave bands interacting with themselves or with below-wave-band motions. When the transport was computed using the full spectrum of motions, including the wave band, it was usually of opposite sign, and was often of similar magnitude, to the wind energy input F_0 .

d. Scaling of TKE and dissipation rate

The relationship between dissipation rate, energy, and a turbulent length scale is a cornerstone of many turbulence closure models [e.g., Tennekes and Lumley (1972)] and can be written

$$\varepsilon = c_\mu^{o(3/4)} \frac{q^3}{\ell}, \quad (22)$$

where ℓ is a turbulent length scale and c_μ^o is an empirical parameter. This definition of c_μ^o follows Burchard (2001) and is commonly used in the k - ε turbulence closure model. By assuming some degree of isotropy, the length scale ℓ can be related to the roll-off wavenumbers of the autospectra of turbulent velocity fluctuations through (17) and is related to the sizes of the eddies that contain the largest fraction of the TKE.

Following Umlauf et al. (2003) and Umlauf and Burchard (2003), one can write

$$\ell = \mathcal{L}|z| \quad (23)$$

and rearrange (22) to get

$$q^3 = \frac{\mathcal{L}}{c_\mu^{o(3/4)}} \varepsilon |z| = \Lambda \varepsilon |z|, \quad (24)$$

where $\Lambda = \mathcal{L}/c_\mu^{o(3/4)}$. In unstratified boundary layers close to a rigid boundary, $\mathcal{L} = \kappa \approx 0.4$. In more complicated boundary layers, but still close to the boundary, two-equation turbulence closure models determine \mathcal{L} using the dynamical length-scale equation. In a boundary layer in which the dissipation of TKE is balanced by flux divergence, Umlauf et al. (2003) and Umlauf and Burchard (2003) suggest that \mathcal{L} approaches 0.2, and they tune the parameters in their models to ensure this. Jones and Monismith (2008a) showed that a one-equation closure model reproduced observations of the turbulence dissipation rate under breaking waves in an estuary by assuming $\ell = 0.25(-z + z_0)$, where z_0 is a roughness length proportional to the significant wave height.

The value of the parameter c_μ^o has been determined to be 0.09 in neutral conditions near a rigid boundary, and has been assumed constant in other conditions (Umlauf and Burchard 2003), but this assumption has not been tested by observations. By making observations of ε , q ,

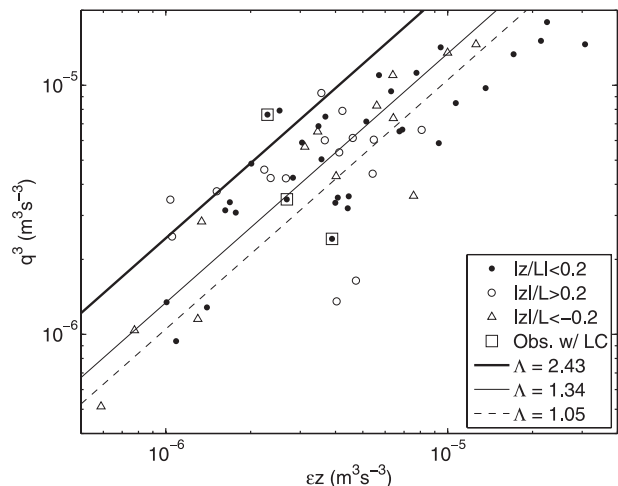


FIG. 11. Test of the standard relationship between TKE, the dissipation rate, and a turbulent length scale. The quantity Λ is equal to $\mathcal{L}/c_\mu^{o(3/4)}$. The lines are standard values (thick line, $c_\mu^o = 0.09$ and $\mathcal{L} = 0.4$), the median of the observations (thin line, $c_\mu^o = 0.2$ and $\mathcal{L} = 0.4$ or $c_\mu^o = 0.09$ and $\mathcal{L} = 0.22$), and the least squares fit to the observations (dashed line, $c_\mu^o = 0.28$ and $\mathcal{L} = 0.4$ or $c_\mu^o = 0.09$ and $\mathcal{L} = 0.17$).

and z , this study makes estimates of the parameter Λ , but does not constrain the distinct values of $c_\mu^{o(3/4)}$ or \mathcal{L} (Fig. 11). Consistent with the findings of Jones and Monismith (2008a), this study finds that observations of Λ in the wave-affected surface layer are smaller than the values expected for turbulence near a rigid boundary. That is, $\Lambda < 0.4/0.09^{3/4}$. Within the context of (17), this means that the length scale of the energy containing eddies, $\lambda_0 = 2\pi/k_0$, is smaller in the ocean surface boundary layer than would be expected based on knowledge of the rigid-boundary turbulence.

4. Discussion

a. Vertical structure of TKE

Section 3c showed that the dissipation rate of TKE is not balanced by local production or growth, so that it must be balanced by the divergence of the flux of TKE. Here, we test an analytic model developed by Craig (1996) and Burchard (2001) that predicts the vertical structure of TKE by solving the TKE equation and assuming a balance of dissipation, shear production, and transport of TKE, which is parameterized with a vertical turbulent diffusivity. This solution has been shown to be consistent with numerical solutions using the full k - ε model (Burchard 2001). Unlike Burchard (2001), but following Craig (1996), we retain the distinction between c_μ and c_μ^o in the solution. The relationship between eddy viscosity, TKE, and dissipation defines c_μ via

$$K_m = c_\mu \frac{q^4}{\varepsilon}. \quad (25)$$

Defining eddy diffusivity of TKE as

$$K_q = \frac{c_\mu q^4}{\sigma_k \varepsilon}, \quad (26)$$

where σ_k is the Schmidt number for TKE, Craig (1996) and Burchard (2001) find

$$\frac{q^3}{u_*^3} = \frac{1}{c_\mu^{o(3/4)}} + G_b \left(\frac{3\sigma_k}{2c_\mu} \right)^{1/2} \left(\frac{|z|}{z_0} \right)^{-m}, \quad (27)$$

where

$$m = \frac{1}{\Lambda} \left(\frac{3\sigma_k}{2c_\mu} \right)^{1/2}. \quad (28)$$

Here, $G_b u_*^3$ is the energy flux into the model domain via breaking waves. The first term on the right-hand-side of (27) is associated with shear production, and the second term is associated with wave breaking.

Two comments are made here regarding the upper boundary in this model. As discussed by Terray et al. (1996) and Gemmrich and Farmer (2004), very near the sea surface, turbulent kinetic energy is injected directly by breaking waves, so the dissipation–transport–production balance is only likely to hold at depths that are below the wave troughs (the wave-affected surface layer). Therefore, the model solved by (27) is not valid above trough level. Accordingly, Burchard (2001) defined the origin of his model domain as being one roughness length below the mean sea surface. We continue to define the origin of our domain as the mean sea surface, a transformation that has been accounted for in (27). Assuming that dissipation is constant in the wave breaking layer, the scaling of Terray et al. (1996) suggests that the upper boundary of the WASL is at $z = z_b = -0.6H_s$, and that one-half of the wind energy input is dissipated in the wave breaking layer, and the other half is exported to the WASL. The total turbulent kinetic energy injected via wave breaking is $F_0 = -G_t \mu_*^3$. If only half of this TKE reaches the WASL, the upper-boundary condition leading to (27) must be $F(z = z_b) = F_0/2 = -G_b \mu_*^3$, where $G_b = G_t/2$. The ratio G_b/G_t is uncertain and is sensitive to the dissipation structure of the wave breaking layer.

Equation (27) does a reasonable job of reproducing the observations, particularly in reproducing the increase in energy at depths shallower than 5 times the significant wave height. However, the details of the agreement are sensitive to the choice of model constants that were discussed in section 3d (Fig. 12). The results

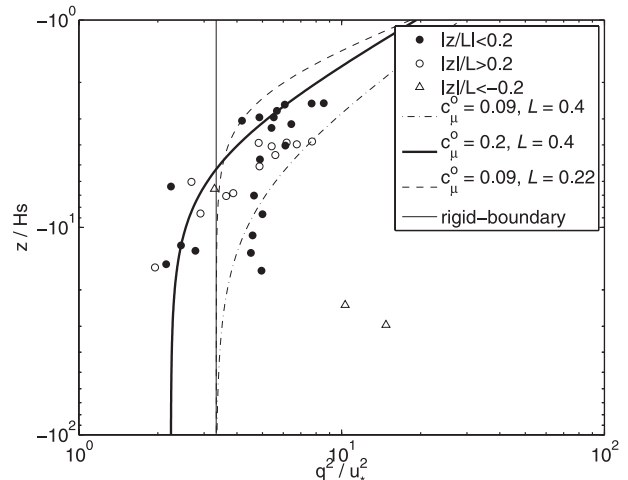


FIG. 12. Comparison of the observed energy profile (symbols) with that expected from analytic solutions to the TKE equation by Craig (1996) and Burchard (2001), and Eq. (27) (lines). These solutions were evaluated with $c_\mu = c_\mu^o$, $\sigma_k = 1$, $z_0 = 0.6H_s$, and $G_b = 84$. Each solution uses different values for \mathcal{L} or each of c_μ and c_μ^o . The thin solid line shows the rigid-boundary scaling used in the k - ε model (Burchard 2001).

presented here use $c_\mu = c_\mu^o$ and $\sigma_k = 1$, as suggested by Burchard, and $z_0 = 0.6H_s$, consistent with Terray et al. (1996) and Soloviev and Lukas (2003). Burchard used a similar value of $z_0 = 0.5H_s$. The parameters c_μ , c_μ^o , and \mathcal{L} have been varied in Fig. 12, but variation of σ_k or of c_μ independently of c_μ^o will also affect the agreement between the model and observations. As suggested for other constants in closure models (Burchard 2001), the best values for c_μ^o and \mathcal{L} may be functions of the relative importance of the local TKE production and flux divergence in the TKE balance. Combining (20), (22), (23), and (27), and ignoring the shear production term in (27), one finds that the scaling of Terray et al. (1996) corresponds to $m = 1$ (Craig 1996). In contrast, the parameters used in Fig. 12 give values of m between 1.7 and 3. Even though the model slope used in (27) is different from the scaling value in (20), the predicted energy and dissipation profiles are somewhat influenced by the shear production term at depths as shallow as twice the significant wave height. This means that the logarithmic slope m is approached only for very shallow observations, of which we have few. Our observations of dissipation rates are in the transition region of the model, where both production and transport of TKE seem to be important. Even given its curved shape at the depths of the observations, the model solution fits the observed dissipation estimates almost as well as the scaling of Terray et al. (1996) (Fig. 9), suggesting that these increased values of m are consistent with observations of the dissipation rate.

For TKE and dissipation rate, the presence of stabilizing ($|z|/L > 0.2$) or destabilizing ($|z|/L < 0.2$) buoyancy forcings did not lead to substantial changes in the results. Observations that might have been expected to be affected by buoyancy forcing are distributed along with those that have minimal buoyancy forcings (Figs. 9, 11, and 12).

b. Effects of wave breaking on turbulent diffusivity

Gerbi et al. (2008) showed that K_h is greater in the ocean surface boundary layer than would be expected using Monin–Obukhov theory (MO), which predicts turbulent diffusivity using buoyancy and momentum fluxes through a rigid boundary. Here, we examine whether the inclusion of wave breaking effects can account for the discrepancy. The sensible heat flux Q_s and the associated diffusivity K_h are defined by

$$Q_s = \rho_0 C_p \overline{T'W'} = -K_h \frac{\partial \bar{T}}{\partial z}, \quad (29)$$

where C_p is the specific heat of water. Monin–Obukhov theory determines the turbulent diffusivity as

$$K_{hMO} = \frac{u_* \kappa |z|}{\phi_h(|z|/L)}, \quad (30)$$

where ϕ_h is the stability function for heat and is a function of buoyancy flux and stress. The stability function ϕ_h is less than one for unstable buoyancy forcing and greater than one for stable buoyancy forcing. Here, we use the definition of ϕ_h as given by Large et al. (1994), which is similar to Beljaars and Holtslag (1991). To calculate $|z|/L$, we use the surface fluxes of heat and momentum, but local application of MO, using local observations of the fluxes (Gerbi et al. 2008), gives nearly identical results. The heat flux predicted by MO is smaller, by a factor of about 2, than the heat flux observed from cospectra (Fig. 13a).

To examine whether wave breaking can explain the difference between the modeled and observed heat fluxes, a term was added to the MO diffusivity. Assuming that $K_h = K_m$, $\mathcal{L} = \kappa$, and ignoring the shear production term in (27), one can combine (22), (23), (25), and (27). Adding this result to (30) gives

$$K_h = u_* \kappa |z| \left\{ \frac{1}{\phi_h} + \frac{1}{c_\mu^{o(3/4)}} \left[G_b c_\mu^{5/2} \left(\frac{3\sigma_k}{2} \right)^{1/2} \left(\frac{z_0}{|z|} \right)^m \right]^{1/3} \right\}. \quad (31)$$

Although not strictly justified from first principles, this addition attempts to incorporate the effects of shear, buoyancy, and wave breaking in a simple way. The heat

fluxes computed using (31) agree with observations much better than do those computed using MO alone, suggesting that wave breaking can account for differences between observed diffusivity and diffusivity predicted from rigid-boundary theories (Fig. 13b). The constants used in this model were $c_\mu = c_\mu^o = 0.2$, and $\sigma_k = 1$. Using $c_\mu^o = 0.09$ had negligible effects on the results.

5. Conclusions

This study estimated selected terms in the turbulent kinetic energy budget of the ocean surface boundary layer: growth of TKE, shear production, Stokes shear production, buoyancy production, and dissipation (Fig. 10). Consistent with previous speculation, the local production terms do not balance dissipation. In the absence of a local balance, it is likely that the enhanced dissipation rates are balanced by the divergence of TKE flux. We were unable to separate turbulence from waves sufficiently to estimate the TKE flux, possibly because turbulent motions explained by wave-band frequencies are important in the TKE flux.

Observations of the dissipation rate are explained well by the scaling of Terray et al. (1996) that relates the dissipation rate to the energy input from the wind to the waves (Fig. 9). The significant wave height used in the scaling must be that of the wind waves, rather than that of the full spectrum. Energy input proportional to u_*^3 gives good agreement between these observations and previous observations. More precise estimates of the energy input from the wind would only have been obtainable with better estimates of the directional wave spectrum and wave growth rate formulas that are well constrained for the complex sea conditions studied here.

As assumed in simplified turbulence closure models, TKE and the dissipation rate in the ocean surface boundary layer are related through a length scale proportional to the distance to the sea surface. However, a proportionality constant smaller by a factor of about 2 than that in rigid-boundary turbulence relates the dissipation rate, depth, and the three-halves power of TKE in the ocean surface boundary layer (Fig. 11).

With an adjusted proportionality between q^3 and εz , the vertical distribution of TKE is reasonably well explained by a one-dimensional model that incorporates the effects of surface gravity waves and shear instabilities (Fig. 12).

Similarly, the vertical turbulent heat flux is predicted well by a one-equation closure model that includes the effects of wave breaking, buoyancy forcing, and shear instability (Fig. 13).

Our estimates of boundary layer turbulence properties were restricted to times of weak to moderate surface

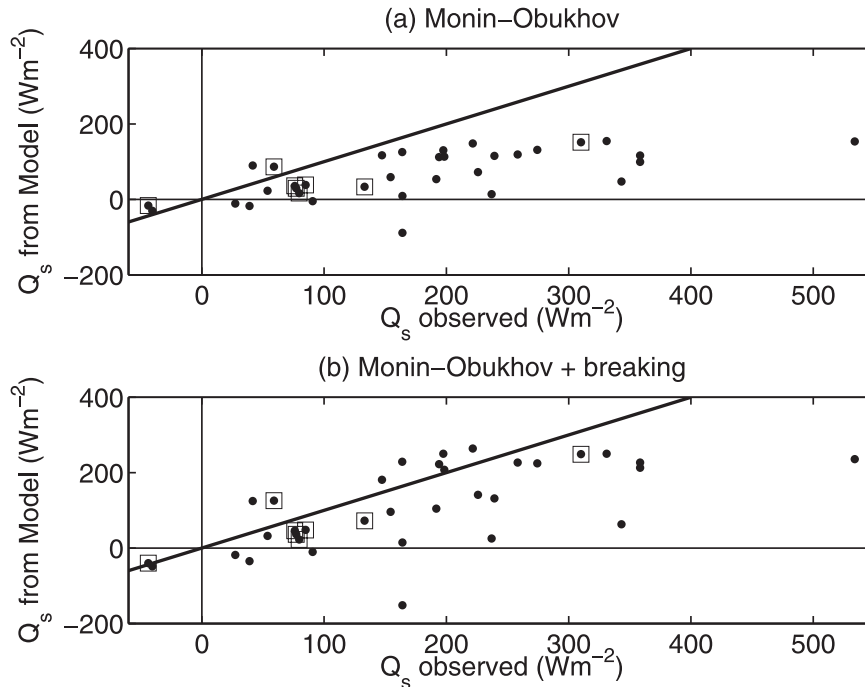


FIG. 13. Vertical heat flux from cospectral observations (Gerbi et al. 2008) and models. The turbulent diffusivities used in modeling the temperature flux are explained in the text. Given the observed temperature gradient, the Monin–Obukhov model underpredicts the temperature fluxes. The composite model accounting for shear instability, buoyancy flux, and wave breaking gives much better agreement with the observations. Boxes show times when Langmuir turbulence was detected at the surface.

forcing. As a result, there were few times when robust Langmuir turbulence was detected concurrently with turbulence energetics. Highlighting the times when Langmuir turbulence was detected did not indicate that it played a distinct role in the energetics or diffusivity. The times when Langmuir turbulence was present did not stand out from the overall distributions when examining the TKE balance or comparing observed and modeled heat fluxes (Figs. 10 and 13). Questions of whether, at what depths, and under what forcing conditions, Langmuir turbulence plays a significant role in surface boundary layer energetics are topics for future research.

The data used to make Figs. 9–13 are available from the authors or online (http://www.whoi.edu/mvco/data/user_data.html). A subset of these data were also printed in Gerbi (2008).

Acknowledgments. Janet Fredericks, Albert J. Williams III, Ed Hobart, and Neil McPhee assisted in the development and deployment of the instruments and the collection of the data. The Office of Naval Research funded this work as a part of CBLAST-Low. Jim Edson led the project and provided data on meteorological forcing. Jim Churchill analyzed the wave measurements. Comments from two anonymous reviewers greatly improved this manuscript.

APPENDIX

Computing Dissipation Rate in Unsteady Advection in Three Directions

At frequencies above the wave band, unsteady advection due to surface waves has predictable effects on turbulence autospectra (Lumley and Terray 1983; Trowbridge and Elgar 2001; Bryan et al. 2003; Feddersen et al. 2007). Methods of evaluating these effects presented by Trowbridge and Elgar (2001), Bryan et al. (2003), and Feddersen et al. (2007) were derived for unidirectional waves. In the presence of multidirectional waves, the equations quantifying the effects of unsteady advection can be written in terms of bounded integrals and a Gaussian, which allows simpler numerical integration than the equations of Feddersen et al. (2007). Equations (A4) and (A5) of Feddersen et al. (2007) are

$$S_{lm}(\omega) = \frac{\alpha \varepsilon^{2/3}}{2(2\pi)^{3/2}} M_{lm}(\omega), \quad (\text{A1})$$

where

$$M_{lm}(\omega) = \int_{-\infty}^{\infty} \int_{-\infty}^{\infty} \int_{-\infty}^{\infty} dk_1 dk_2 dk_3 \frac{k^{-11/3} \left(\delta_{lm} - \frac{k_l k_m}{k^2} \right)}{\sqrt{\sigma_i^2 k_i^2}} \exp \left[-\frac{(k_1 \bar{u}_1 + k_2 \bar{u}_2 - \omega)^2}{2\sigma_i^2 k_i^2} \right]. \tag{A2}$$

The coordinate system is defined such that the x_3 direction is vertical, and x_1 and x_2 are the principal axes of the wave motion. The scalar wavenumber magnitude is $k^2 = k_1^2 + k_2^2 + k_3^2$, δ_{lm} is the Kronecker delta function, σ_i^2 is the variance of the wave velocities, and the covariances of the wave velocity in this coordinate system are zero. The following substitutions are made:

$$\mathbf{k} = (k_1, k_2, k_3) = \omega r \left(\frac{\sin \theta \cos \phi}{\sigma_1}, \frac{\sin \theta \sin \phi}{\sigma_2}, \frac{\cos \theta}{\sigma_3} \right). \tag{A3}$$

Note that these substitutions differ slightly from those made by Feddersen et al. (2007) and that the normalization fails if any of $(\sigma_1, \sigma_2, \sigma_3)$ is zero. Under this transformation,

$$\sigma_i^2 k_i^2 = \omega^2 r^2 \quad \text{and} \tag{A4}$$

$$dk_1 dk_2 dk_3 = \frac{\omega}{\sigma_1 \sigma_2 \sigma_3} r^2 \sin \theta d\phi d\theta d\phi. \tag{A5}$$

Here, r is defined in the interval between 0 and ∞ , ϕ between 0 and 2π , and θ between 0 and π . The following functions are defined:

$$R = \frac{1}{r}, \tag{A6}$$

$$G^2 = \sin^2 \theta \left(\frac{\cos^2 \phi}{\sigma_1^2} + \frac{\sin^2 \phi}{\sigma_2^2} \right) + \frac{\cos^2 \theta}{\sigma_3^2}, \quad \text{and} \tag{A7}$$

$$P_{lm} = \delta_{lm} - \frac{k_l k_m}{k^2}. \tag{A8}$$

With these definitions,

$$k^2 = \frac{\omega^2 G^2}{R^2}. \tag{A9}$$

Like G , the phase function P is a function only of θ and ϕ . For example, in the vertical direction,

$$P_{33} = \frac{\sin^2 \theta}{G^2} \left(\frac{\cos^2 \phi}{\sigma_1^2} + \frac{\sin^2 \phi}{\sigma_2^2} \right). \tag{A10}$$

Making the appropriate substitutions and continuing with the algebra, one finds

$$M_{lm} = \frac{1}{\omega^{5/3}} \frac{1}{\sigma_1 \sigma_2 \sigma_3} \int_0^\pi d\theta \int_0^\pi d\phi G^{-11/3} \sin \theta P_{lm} \times \int_0^\infty dR R^{2/3} \exp \left[-\frac{(R_0 - R)^2}{2} \right], \tag{A11}$$

where

$$R_0 = \frac{\bar{u}_1}{\sigma_1} \sin \theta \cos \phi + \frac{\bar{u}_2}{\sigma_2} \sin \theta \sin \phi. \tag{A12}$$

Finally, we define

$$J_{lm} = M_{lm} \frac{\omega^{5/3}}{2(2\pi)^{3/2}} = \frac{1}{2(2\pi)^{3/2}} \frac{1}{\sigma_1 \sigma_2 \sigma_3} \int_0^\pi d\theta \times \int_0^{2\pi} d\phi G^{-11/3} \sin \theta P_{lm} \int_0^\infty dR R^{2/3} \exp \left[-\frac{(R_0 - R)^2}{2} \right] \tag{A13}$$

and substitute into (A1) to get

$$S_{lm}(\omega) = \frac{\alpha e^{2/3}}{\omega^{5/3}} J_{lm}(\omega). \tag{A14}$$

Equation (A13) was integrated numerically, and we tested our integration scheme in two ways. First, although no simpler computationally, the R integral in (A13) can be written in terms of parabolic cylinder functions. Evaluation of J_{lm} using our integration method and using parabolic cylinder functions showed no discernible difference. Second, in the no-current limit with $\sigma_1 = \sigma_2 = \sigma_3 = \sigma_0$, there is an analytic solution for the fully contracted form $M_{ll} = M_{11} + M_{22} + M_{33}$,

$$M_{ll} = \frac{\sigma_0^{2/3}}{\omega^{5/3}} \Gamma \left(\frac{5}{6} \right) 2^{17/6} \pi, \tag{A15}$$

that we also were able to match with our numerical integration.

REFERENCES

Agrawal, Y. C., E. A. Terray, M. A. Donelan, P. A. Hwang, A. J. Williams III, W. M. Drennan, K. K. Kahma, and S. A. Kitaigorodskii, 1992: Enhanced dissipation of kinetic energy beneath surface waves. *Nature*, **359**, 219–220.

- Anis, A., and J. N. Moum, 1995: Surface wave–turbulence interactions: Scaling $\varepsilon(z)$ near the sea surface. *J. Phys. Oceanogr.*, **25**, 2025–2044.
- Batchelor, G. K., 1982: *The Theory of Homogeneous Turbulence*. Cambridge University Press, 197 pp.
- Beljaars, A. C. M., and A. A. M. Holtslag, 1991: Flux parameterization over land surfaces for atmospheric models. *J. Appl. Meteor.*, **30**, 327–341.
- Bryan, K. R., K. P. Black, and R. M. Gorman, 2003: Spectral estimates of dissipation rate within and near the surf zone. *J. Phys. Oceanogr.*, **33**, 979–993.
- Burchard, H., 2001: Simulating the wave-enhanced layer under breaking surface waves with two-equation turbulence models. *J. Phys. Oceanogr.*, **31**, 3133–3145.
- , and H. Baumert, 1995: On the performance of a mixed-layer model based on the $k \varepsilon$ turbulence closure. *J. Geophys. Res.*, **100**, 8523–8540.
- Churchill, J. H., A. J. Plueddemann, and S. M. Faluotico, 2006: Extracting wind sea and swell from directional wave spectra derived from a bottom-mounted ADCP. Woods Hole Oceanographic Institution Tech. Rep. 200613, 34 pp.
- Corrsin, S., and A. L. Kistler, 1955: Free-stream boundaries of turbulent flows. National Advisory Committee on Aeronautics Rep. 1244, Washington, DC, 32 pp.
- Craig, P. D., 1996: Velocity profiles and surface roughness under breaking waves. *J. Geophys. Res.*, **101** (C1), 1265–1277.
- , and M. L. Banner, 1994: Modeling wave-enhanced turbulence in the ocean surface layer. *J. Phys. Oceanogr.*, **24**, 2546–2559.
- Crawford, C. B., and D. M. Farmer, 1987: On the spatial distribution of ocean bubbles. *J. Geophys. Res.*, **92** (C8), 8231–8243.
- D’Asaro, E., 2001: Turbulent vertical kinetic energy in the ocean mixed layer. *J. Phys. Oceanogr.*, **31**, 3530–3537.
- Donelan, M. A., 1999: Wind-induced growth and attenuation of laboratory waves. *Wind-over-wave Couplings. Perspectives and Prospects*, S. G. Sajjadi, N. H. Thomas, and J. C. R. Hunt, Eds., Clarendon Press, 183–194.
- , and W. J. Pierson, 1987: Radar scattering and equilibrium ranges in wind generated waves with applications to scatterometry. *J. Geophys. Res.*, **92**, 4971–5029.
- , A. V. Babanin, I. R. Young, and M. L. Banner, 2006: Wave-follower field measurements of the wind-input spectral function. Part II: Parameterization of the wind input. *J. Phys. Oceanogr.*, **36**, 1672–1689.
- Drennan, W. M., M. A. Donelan, E. A. Terray, and K. B. Katsaros, 1996: Oceanic turbulence dissipation measurements in SWADE. *J. Phys. Oceanogr.*, **26**, 808–815.
- Feddersen, F., J. H. Trowbridge, and A. J. Williams III, 2007: Vertical structure of dissipation in the nearshore. *J. Phys. Oceanogr.*, **37**, 1764–1777.
- Fung, J. C. H., J. C. R. Hunt, N. A. Malik, and R. J. Perkins, 1992: Kinematic simulation of homogeneous turbulence by unsteady random Fourier modes. *J. Fluid Mech.*, **236**, 281–318.
- Gemmrich, J. R., and D. M. Farmer, 2004: Near-surface turbulence in the presence of breaking waves. *J. Phys. Oceanogr.*, **34**, 1067–1086.
- Gerbi, G. P., 2008: Observations of turbulent fluxes and turbulence dynamics in the ocean surface boundary layer. Ph.D. thesis, Woods Hole Oceanographic Institution–Massachusetts Institute of Technology, Woods Hole, MA, 119 pp.
- , J. H. Trowbridge, J. B. Edson, A. J. Plueddemann, E. A. Terray, and J. J. Fredericks, 2008: Measurements of momentum and heat transfer across the air–sea interface. *J. Phys. Oceanogr.*, **38**, 1054–1072.
- Greenan, B. J., N. S. Oakey, and F. W. Dobson, 2001: Estimates of dissipation in the ocean mixed layer using a quasi-horizontal microstructure profiler. *J. Phys. Oceanogr.*, **31**, 992–1004.
- Hannoun, I. A., H. J. S. Fernando, and E. J. List, 1988: Turbulence structure near a sharp density interface. *J. Fluid Mech.*, **180**, 189–209.
- Hanson, J. L., and O. M. Phillips, 2001: Automated analysis of ocean surface directional wave spectra. *J. Atmos. Oceanic Technol.*, **18**, 277–293.
- Jones, N. L., and S. G. Monismith, 2008a: Modeling the influence of wave-enhanced turbulence in a shallow tide- and wind-driven water column. *J. Geophys. Res.*, **113**, C03009, doi:10.1029/2007JC004246.
- , and —, 2008b: The influence of whitecapping waves on the vertical structure of turbulence in a shallow estuarine environment. *J. Phys. Oceanogr.*, **38**, 1563–1580.
- Jones, W. P., and B. E. Launder, 1972: The prediction of laminarization with a two-equation model of turbulence. *Int. J. Heat Mass Transfer*, **15**, 301–314.
- Kaimal, J., J. C. Wyngaard, Y. Izumi, and O. R. Cote, 1972: Spectral characteristics of surface-layer turbulence. *Quart. J. Roy. Meteor. Soc.*, **98**, 563–589.
- Kantha, L. H., and C. A. Claydon, 2004: On the effect of surface gravity waves on mixing in the oceanic mixed layer. *Ocean Modell.*, **6**, 101–124.
- Kitaigorodskii, S. A., M. A. Donelan, J. L. Lumley, and E. A. Terray, 1983: Wave–turbulence interactions in the upper ocean. Part II: Statistical characteristics of wave and turbulent components of the random velocity field in the marine surface layer. *J. Phys. Oceanogr.*, **13**, 1988–1999.
- Klebanoff, P. S., 1955: Characteristics of turbulence in a boundary layer with zero pressure gradient. National Advisory Committee on Aeronautics Rep. 1247, Washington, DC, 19 pp.
- Kolmogorov, A. N., 1941a: Dissipation of energy in the locally isotropic turbulence. *Dokl. Akad. Nauk SSSR*, **31**, 538–540.
- , 1941b: The local structure of turbulence in incompressible viscous fluid for very large Reynolds numbers. *Dokl. Akad. Nauk SSSR*, **30**, 301–305.
- Krogstad, H., R. Gordon, and M. Miller, 1988: High-resolution directional wave spectra from horizontally mounted acoustic Doppler current meters. *J. Atmos. Oceanic Technol.*, **5**, 340–352.
- Large, W. G., J. C. McWilliams, and S. C. Doney, 1994: Oceanic vertical mixing: A review and a model with a nonlocal boundary layer parameterization. *Rev. Geophys.*, **32**, 363–403.
- Lentz, S. J., 1992: The surface boundary layer in coastal upwelling regions. *J. Phys. Oceanogr.*, **22**, 1517–1539.
- Li, M., C. Garrett, and E. Skillingstad, 2005: A regime diagram for classifying turbulent large eddies in the upper ocean. *Deep-Sea Res. I*, **52**, 259–278.
- Lumley, J., and E. Terray, 1983: Kinematics of turbulence convected by a random wave field. *J. Phys. Oceanogr.*, **13**, 2000–2007.
- McPhee, M. G., and J. D. Smith, 1976: Measurements of the turbulent boundary layer under pack ice. *J. Phys. Oceanogr.*, **6**, 696–711.
- McWilliams, J. C., P. P. Sullivan, and C.-H. Moeng, 1997: Langmuir turbulence in the ocean. *J. Fluid Mech.*, **334**, 1–30.
- Mellor, G. L., and T. Yamada, 1982: Development of a turbulence closure model for geophysical fluid problems. *Rev. Geophys.*, **20**, 851–875.

- Melville, W. K., F. Veron, and C. J. White, 2002: The velocity field under breaking waves: Coherent structures and turbulence. *J. Fluid Mech.*, **454**, 203–233.
- Nezu, I., and W. Rodi, 1986: Open-channel flow measurements with a laser Doppler anemometer. *J. Hydraul. Eng.*, **112**, 335–355.
- Noh, Y., H. S. Min, and S. Raasch, 2004: Large eddy simulation of the ocean mixed layer: The effects of wave breaking and Langmuir circulation. *J. Phys. Oceanogr.*, **34**, 720–735.
- Plant, W. J., 1982: A relationship between wind stress and wave slope. *J. Geophys. Res.*, **87**, 1961–1967.
- Plueddemann, A. J., and R. A. Weller, 1999: Structure and evolution of the oceanic surface boundary layer during the Surface Waves Processes Program. *J. Mar. Syst.*, **21**, 85–102.
- , J. A. Smith, D. M. Farmer, R. A. Weller, W. R. Crawford, R. Pinkel, S. Vagle, and A. Gnanadesikan, 1996: Structure and variability of Langmuir circulation during the Surface Waves Processes Program. *J. Geophys. Res.*, **101** (C2), 3525–3543.
- , E. A. Terray, and R. Merrewether, 2001: Design and performance of a self-contained fan-beam ADCP. *IEEE J. Oceanic Eng.*, **26**, 54–59.
- Santala, M. J., 1991: Surface-referenced current meter measurements. Ph.D. thesis, Woods Hole Oceanographic Institution—Massachusetts Institute of Technology, Woods Hole, MA, 280 pp.
- Skylingstad, E. D., and D. W. Denbo, 1995: An ocean large-eddy simulation of Langmuir circulation and convection in the surface mixed layer. *J. Geophys. Res.*, **100** (C5), 8501–8522.
- Smith, J. A., 1992: Observed growth of Langmuir circulation. *J. Geophys. Res.*, **97**, 5651–5664.
- Soloviev, A., and R. Lukas, 2003: Observation of wave-enhanced turbulence in the near-surface layer of the ocean during TOGA COARE. *Deep-Sea Res. I*, **50**, 371–395.
- Stips, A., H. Burchard, K. Bolding, H. Prandke, A. Simon, and A. Wuest, 2005: Measurement and simulation of viscous dissipation in the wave affected surface layer. *Deep-Sea Res. II*, **52**, 1133–1155.
- Strong, B., B. Brumley, E. A. Terray, and G. W. Stone, 2000: The performance of ADCP-derived wave directional spectra and comparison with other independent measurements. *Proc. Oceans 2000*, Providence, RI, MTS/IEEE, 1195–1203.
- Sullivan, P. P., J. C. McWilliams, and W. K. Melville, 2007: Surface gravity wave effects in the oceanic boundary layer: Large-eddy simulation with vortex force and stochastic breakers. *J. Fluid Mech.*, **593**, 405–452.
- Taylor, G. I., 1938: The spectrum of turbulence. *Proc. Roy. Soc. London*, **164A**, 476–490.
- Tennekes, H., and J. L. Lumley, 1972: *A First Course in Turbulence*. Massachusetts Institute of Technology Press, 300 pp.
- Terray, E. A., M. A. Donelan, Y. C. Agrawal, W. M. Drennan, K. K. Kahma, A. J. Williams III, P. A. Hwang, and S. A. Kitaigorodskii, 1996: Estimates of kinetic energy dissipation under breaking waves. *J. Phys. Oceanogr.*, **26**, 792–807.
- , B. H. Brumley, and B. Strong, 1999a: Measuring waves and currents with and upward-looking ADCP. *Proc. Sixth Working Conf. on Current Measurements*, San Diego, CA, IEEE, 66–71.
- , W. M. Drennan, and M. A. Donelan, 1999b: The vertical structure of shear and dissipation in the ocean surface layer. *Proc. Symp. on the Wind-driven Air–Sea Interface—Electromagnetic and Acoustic Sensing, Wave Dynamics, and Turbulent Fluxes*, Sydney, NSW, Australia, University of New South Wales, 239–245.
- Thompson, S. M., and J. S. Turner, 1975: Mixing across an interface due to turbulence generated by an oscillating grid. *J. Fluid Mech.*, **67**, 349–368.
- Thomson, R. E., and I. V. Fine, 2003: Estimating mixed layer depth from oceanic profile data. *J. Atmos. Oceanic Technol.*, **20**, 319–329.
- Trowbridge, J., and S. Elgar, 2001: Turbulence measurements in the surf zone. *J. Phys. Oceanogr.*, **31**, 2403–2417.
- Tseng, R.-S., and E. D’Asaro, 2004: Measurements of turbulent vertical kinetic energy in the ocean mixed layer from Lagrangian floats. *J. Phys. Oceanogr.*, **34**, 1984–1990.
- Umlauf, L., and H. Burchard, 2003: A generic length-scale equation for geophysical turbulence models. *J. Mar. Res.*, **61**, 235–265.
- , —, and K. Hutter, 2003: Extending the $k\omega$ turbulence model towards oceanic applications. *Ocean Modell.*, **5**, 195–218.
- Veron, F., and W. K. Melville, 2001: Experiments on the stability and transition of wind-driven water surfaces. *J. Fluid Mech.*, **446**, 25–65.
- Wilcox, D., 1988: Reassessment of the scale-determining equation for advanced turbulence models. *AIAA J.*, **26**, 1299–1310.